

Weibel Instability in Collisionless Plasmas Across Astrophysical and Laboratory Shocks

Vivek Shrivastav,^{1, a)} Mani K Chettri,¹ Hemam D Singh,² Britan Singh,¹ and Rupak Mukherjee^{1, b)}

¹⁾*Department of Physics, Sikkim University, Gangtok, India, 737102*

²⁾*Department of Physics, Netaji Subhas University of Technology, New Delhi, India, 110078*

We present a systematic cold-fluid analysis of the purely transverse Weibel (current-filamentation) instability across four regimes: non-relativistic (NR) single-species, NR multi-species, relativistic single-species, and relativistic multi-species (electron–positron and electron–proton). Beginning from the linearized fluid equations, we derive the quartic dispersion relations in each regime, reduce them to standard quadratics in ω^2 , and extract explicit scaling laws for the maximum growth rate γ_{\max} and characteristic unstable wavenumber $k_{\max} = \omega_{pi}/c$. The main analytical contributions are: (i) explicit regime-transition criteria in the $(v_0/c, m_i/m_e)$ parameter space, quantifying the error from applying a simpler formula outside its domain of validity; (ii) contour maps of relativistic suppression and mass-ratio dependence that serve directly as diagnostic charts; and (iii) an assessment of where in parameter space the purely transverse mode dominates over competing oblique and two-stream instabilities. Relativistic corrections suppress γ_{\max} by up to 40 per cent, becoming significant above $v_0 \approx 0.2c$ and reaching maximum suppression near $v_0 \approx 0.9c$. For the tabletop laser experiment by Bai et al. (2025, *Nat. Commun.* **16**, 3770), the cold-fluid prediction gives $d_i = c/\omega_{pi} \approx 31.7 \mu\text{m}$, in excellent agreement (within 2 per cent) with the measured filament spacing $\lambda_F \approx 31 \mu\text{m}$. The saturation field estimate $B_{\text{sat}} \sim \sqrt{\mu_0 n_i m_i} v_0 \approx 2.3 \times 10^4 \text{ T}$ is a cold-fluid upper bound, consistent with the measured $\approx 5000 \text{ T}$ within the expected kinetic suppression. In-situ comparison with two MMS burst-mode bow shock crossing events (2015 October 16 and 2017 November 25) is presented in Section IV. Both events confirm the cold-fluid scale prediction $k_{\max} d_i = 1$ from FGM/FPI PySPEDAS data; the upstream ion skin depths ($d_i = 51 \text{ km}$ and 62 km respectively) lie within a factor of 2 of the spectral break in the perpendicular magnetic field power spectrum, consistent with Kropotina et al.¹. The multi-environment scatter plot spans 21 orders of magnitude in n_i , from the laser-plasma ($d_i \approx 32 \mu\text{m}$) to young SNR scales, with all points lying within a factor of 3 of the 1:1 line.

I. INTRODUCTION

Collisionless shocks appear in many astrophysical environments. They form in gamma-ray burst (GRB) afterglows where relativistic ejecta drive into the interstellar medium at Lorentz factors $\Gamma \sim 10\text{--}100$ ^{2,3}; in young supernova remnants (SNRs) expanding at $v_{\text{sh}} \sim 10^4 \text{ km s}^{-1}$ ⁴; in pulsar wind nebulae driven by ultra-relativistic pair winds⁵; and at planetary bow shocks formed by the solar wind^{6,7}. In these environments, binary collisions between particles are negligible. Yet sharp shock transitions with large density and pressure jumps do exist. These shocks are maintained by plasma instabilities that generate magnetic turbulence on scales close to the ion inertial length $d_i = c/\omega_{pi}$, providing an effective collisionality⁸.

The Weibel instability, also known as the current-filamentation instability, is one mechanism for this process^{2,9,10}. When two plasma populations stream through each other, the velocity anisotropy drives exponentially growing transverse electromagnetic perturbations. The plasma organises into current filaments and the magnetic field grows until the ion gyroradius becomes comparable to the filament spacing, at which point the shock transition is established^{11,12}. Particle-in-cell (PIC) simulations confirm this picture across a wide range of shock velocities^{6,10,11,13}.

A two-beam plasma is, however, unstable to a spectrum of modes beyond the purely transverse Weibel mode. These include the longitudinal two-stream (electrostatic) mode, the

oblique electromagnetic-filamentation mode, and the Bell and Buneman modes in the presence of a background magnetic field or current. Bret¹⁴ performed a comprehensive three-dimensional analysis of all these modes and showed that in the sub-relativistic regime ($v_0 \lesssim 0.2c$) with a symmetric cold-beam configuration, the transverse filamentation (Weibel) mode typically has the highest growth rate among electromagnetic modes. At mildly relativistic velocities ($v_0 \sim 0.2\text{--}0.5c$), oblique modes can become competitive. At highly relativistic velocities, the maximum growth often shifts to oblique modes. We analyse only the transverse Weibel mode in this paper, restricting to $v_0 \lesssim 0.2c$ where this mode dominates; the full justification and parameter boundaries are given in Section VI B.

Direct laboratory evidence has come from large laser facilities. Huntington et al.¹⁵ observed Weibel magnetic field generation in counterstreaming plasmas at OMEGA and NIF. Fox et al.¹⁶ reported filamentation in laser-driven plasmas at OMEGA EP. Manuel et al.¹⁷ studied the saturation of ion-Weibel fields in CH, Al, and Cu counterstreaming experiments. Most recently, Bai et al.¹⁸ showed that a Weibel-mediated collisionless shock can be produced with a compact tabletop femtosecond laser operating at $v_{\text{sh}} \approx 0.03c$, greatly reducing the experimental requirements. The expanding geometry of laser-produced plasmas and the role of density gradients in modifying the Weibel spectrum have been analysed in detail by Kocharovsky et al.¹⁹.

Spacecraft data at Earth's bow shock provide an independent in-situ test. The NASA Magnetospheric Multi-scale (MMS) mission⁷ provides burst-mode measurements that resolve scales down to the electron inertial length. Two separate MMS bow shock events are analysed here us-

^{a)}Email: vivekshrivastav1998@gmail.com

^{b)}Corresponding author: rmukherjee@cus.ac.in

ing PySPEDAS²⁰. The first is a 2015 October 16 quasi-perpendicular crossing with moderate parameters ($M_A \approx 2.4$, $\beta_i \approx 9.0$, upstream $d_i \approx 51$ km). The second is a 2017 November 25 crossing ($M_A \approx 2.3$, $\beta_i \approx 2.4$, upstream $d_i \approx 62$ km) associated with the event studied by Kropotina et al.¹ using hybrid kinetic simulations. The full in-situ comparison—including FGM/FPI timeseries, B_\perp power spectra, and a multi-environment d_i scatter plot spanning 21 orders of magnitude—is presented in Section IV.

The present work derives and applies the cold-fluid Weibel dispersion relations across these four regimes. Its contributions are as follows. First, it provides explicit numerical criteria for when each regime formula fails and by how much (Section V), filling a gap between the individual papers that treat each regime separately. Second, it maps the relativistic suppression and mass-ratio dependence as two-dimensional contour charts (Figs 6 and 9) that can be used directly as diagnostic tools without recomputing the dispersion relation. Third, it applies these maps to assess where the transverse Weibel mode dominates over competing modes (Section VI B). Fourth, it validates the scale prediction $k_{\max} = \omega_{pi}/c$ with the Bai et al. experiment (Section III) and provides a quantitative assessment of the cold-fluid framework’s reliability and limitations.

The paper is organised as follows. Section II gives the four dispersion relations. Section III applies them to the Bai et al. experiment, including the saturation field and shock formation time. Section IV presents the MMS in-situ comparison. Section V shows the full growth rate curves and parameter-space maps. Section VI discusses regime boundaries, competing instabilities, and the limits of the cold-fluid approach. Section VII gives the conclusions.

II. FLUID DISPERSION THEORY OF THE WEIBEL INSTABILITY

A. Physical Setup and Notation

We consider a collisionless, unmagnetised plasma where two equal-density beams stream in opposite directions along \hat{z} at velocities $+v_0\hat{z}$ and $-v_0\hat{z}$. A transverse magnetic perturbation propagates along \hat{x} , perpendicular to the drift. The Lorentz force $\vec{v} \times \vec{B}$ deflects charged particles transversely, creating current bunching that reinforces the perturbation through Ampère’s law and causes exponential growth of current filaments. To find the growing mode we substitute $\omega = i\gamma$ (purely imaginary frequency) into the dispersion relations derived below.

Throughout, the species plasma frequency is defined as $\omega_{ps} = \sqrt{n_s e^2 / m_s \epsilon_0}$, where n_s is the total number density of species s (i.e. summed over both beams, so that $n_s = 2n_{0s}$ with n_{0s} the per-beam density). All derivations below assume equal and symmetric beam densities ($n_{0b} = n_{0p} = n_0$), so that $n_{\text{total}} = 2n_0$ for each species. In realistic laser-plasma or bow-shock configurations, the reflected/beam population often has density much smaller than the background ($n_{\text{beam}}/n_{\text{bg}} \ll 1$), which reduces γ_{\max} and shifts k_{\max} ²¹; the symmetric equal-

density case treated here gives the maximum growth rate for a given total density.

The single-species dispersion relation derived in Section II B is general for any charged species. When the instability is driven by ion beams rather than electron beams, m_e is replaced by m_i and ω_{pe} by ω_{pi} throughout.

The Lorentz factor of a beam with velocity v_0 is denoted $\Gamma_0 = (1 - v_0^2/c^2)^{-1/2}$. In the multi-species case, each species has its own Lorentz factor, $\Gamma_{0e} = (1 - v_{0e}^2/c^2)^{-1/2}$ for electrons and $\Gamma_{0i} = (1 - v_{0i}^2/c^2)^{-1/2}$ for ions. We reserve γ for the instability growth rate.

The four regimes and their leading-order scaling laws are listed in Table I.

TABLE I: The four regimes of the cold-fluid Weibel instability analysed in this work. Here $\omega_{ps} = \sqrt{n_s e^2 / m_s \epsilon_0}$ is defined with the total species density $n_s = 2n_0$. The symbol ω_p denotes the plasma frequency of the driving species: ω_{pe} for electron-driven and ω_{pi} for ion-driven cases.

Leading-order scaling laws are in the non-relativistic limit $v_0 \ll c$.

Regime	γ_{\max} (leading order)	k_{\max}
NR single-species	$\approx 0.7 \omega_p (v_0/c)$	$\approx \omega_p/c$
NR multi-species	$\approx 0.7 (\omega_{pe}^2 + \omega_{pi}^2)^{1/2} (v_0/c)$	$\approx (\omega_{pe}^2 + \omega_{pi}^2)^{1/2} / c$
Rel. single-species	$\sim \omega_p (v_0/c) / \Gamma_0^{3/2}$	$\sim \omega_p / (c \Gamma_0^{1/2})$
Rel. multi-species	both species suppressed by Γ_{0e}, Γ_{0i}	shifted to lower k

B. Non-Relativistic Single-Species Case

We consider a collisionless, non-relativistic two-fluid plasma with no background magnetic field. The beam drifts in the \hat{z} -direction with velocity $v_{0b}\hat{z}$, and the return population drifts in the opposite direction with velocity $\vec{v}_{0p} = -v_{0b}\hat{z}$. The fluctuating electric field is $\vec{E}_1 = E_1\hat{z}$, and the magnetic field perturbation propagates along \hat{x} : $\vec{B}_1 = B_1(x)\hat{y}$ ($\vec{k} = k\hat{x}$).

Writing the total beam velocity as $\vec{v}_b = v_{0b}\hat{z} + \vec{v}_{1b}$ and linearising the equation of motion:

$$\frac{\partial \vec{v}_{1b}}{\partial t} + (\vec{v}_{0b} \cdot \nabla) \vec{v}_{1b} = \frac{q_s \vec{E}_1}{m_s} + \frac{q_s \vec{v}_{0b} \times \vec{B}_1}{m_s}, \quad (1)$$

where q_s and m_s are the charge and mass of the driving species (for electrons, $q_s = -e$). Assuming $f_1 \sim e^{i(kx - \omega t)}$, the x - and z -components of Eq. (1) give $v_{1bx} = -(q_s / im_s \omega) v_{0b} B_{1y}$ and $v_{1bz} = -q_s E_{1z} / (im_s \omega)$. From Faraday’s law, $B_{1y} = -(k/\omega) E_{1z}$, so

$$v_{1bx} = \frac{q_s E_{1z}}{m_s \omega} \frac{kv_{0b}}{i\omega}. \quad (2)$$

The linearised continuity equation after Fourier transform yields $n_{1b} = n_0(k/\omega) v_{1bx}$, where n_0 is the per-beam density. The x -components of the beam and return-population current

densities cancel by symmetry, leaving only the z -component of the total current:

$$\vec{J} = -2 \frac{n_0 q_s^2}{i m_s \omega} E_1 \left(1 + \frac{k^2 v_0^2}{\omega^2} \right) \hat{z}. \quad (3)$$

Applying Ampère's law in the z -direction and substituting Eq. (3), with $\omega_p = \sqrt{2n_0 q_s^2 / m_s \epsilon_0} = \sqrt{n_s q_s^2 / m_s \epsilon_0}$ (where $n_s = 2n_0$ is the total species density), gives the dispersion relation

$$\omega^4 - \omega^2(\omega_p^2 + k^2 c^2) - \omega_p^2 k^2 v_0^2 = 0. \quad (4)$$

Setting $\omega = i\gamma$ and expanding to leading order in v_0^2/c^2 :

$$\gamma \approx \omega_p \frac{v_0}{c} \left(1 + \frac{\omega_p^2}{k^2 c^2} \right)^{-1/2}. \quad (5)$$

This function rises monotonically from zero at $k = 0$ and saturates asymptotically at $\omega_p v_0 / c$ for $k \gg \omega_p / c$; there is no local maximum in k . Following standard convention, the half-saturation point defines $k_{\max} = \omega_p / c$, giving

$$\gamma(k_{\max}) \approx \frac{1}{\sqrt{2}} \omega_p \frac{v_0}{c} \approx 0.7 \omega_p \frac{v_0}{c}, \quad (6)$$

with the true asymptotic maximum $\gamma_{\max} = \omega_p v_0 / c$ approached at $k \gg \omega_p / c$. This result is standard^{9,22,23}. Following Kropotina et al.¹, this cold-fluid result gives γ_{\max} as an upper bound; kinetic corrections reduce the actual rate when $v_{\text{th}} \gtrsim v_0$, while k_{\max} is less sensitive to such corrections.

C. Non-Relativistic Multi-Species Case

We now include the ion beam, which drifts at $\pm v_{0i} \hat{z}$. The derivation follows Section II B for each species independently. The x -current components again cancel by symmetry, and the combined current density is

$$\vec{J} = -2 \frac{n_{0e} e^2}{m_e i \omega} E_1 \left(1 + \frac{k^2 v_{0e}^2}{\omega^2} \right) \hat{z} - 2 \frac{n_{0i} e^2}{m_i i \omega} E_1 \left(1 + \frac{k^2 v_{0i}^2}{\omega^2} \right) \hat{z}. \quad (7)$$

Applying Ampère's law yields the multi-species dispersion relation:

$$\omega^4 - \omega^2(\omega_{pe}^2 + \omega_{pi}^2 + k^2 c^2) - (\omega_{pe}^2 k^2 v_{0e}^2 + \omega_{pi}^2 k^2 v_{0i}^2) = 0. \quad (8)$$

For a realistic electron–proton plasma, $\omega_{pi} / \omega_{pe} = \sqrt{m_e / m_i} \approx 0.023$, so the ion contribution is negligible. For electron–positron pairs ($m_e = m_i$), both species contribute equally and γ_{\max} is higher.

D. Relativistic Single-Species Case

When beam velocities approach c , the relativistic momentum $\vec{P} = m_s \Gamma_0 \vec{v}$ replaces the classical momentum. The relativistic equation of motion is

$$\frac{\partial \vec{P}}{\partial t} + (\vec{v} \cdot \nabla) \vec{P} = q_s (\vec{E}_1 + \vec{v} \times \vec{B}_1). \quad (9)$$

Using the identity $\partial \Gamma / \partial v_z = \Gamma^3 v_z / c^2$, linearisation of the z -component of Eq. (9) gives $v_{1bz} = q_s E_{1z} / (i m_s \Gamma_0^3 \omega)$, while the x -component gives $v_{1bx} = q_s v_0 k E_{1z} / (m_s \Gamma_0 \omega \cdot i \omega)$. Following the same current-assembly procedure as Section II B, the relativistic single-species dispersion relation is

$$\omega^4 - \omega^2 \left(k^2 c^2 + \frac{\omega_p^2}{\Gamma_0^3} \right) - \frac{\omega_p^2 k^2 v_0^2}{\Gamma_0} = 0. \quad (10)$$

Comparing with Eq. (4), the Lorentz factor Γ_0 appears in the denominator of both the restoring term (with Γ_0^3 , from the longitudinal effective mass) and the drive term (with Γ_0 , from the transverse effective mass). This is the physical origin of relativistic suppression. At $v_0 \approx 0.9c$ ($\Gamma_0 \approx 2.3$), γ_{\max} is reduced by about 40 per cent relative to the non-relativistic prediction^{21,24}.

E. Relativistic Multi-Species Case

Extending the relativistic treatment to both electrons and ions, the combined dispersion relation is

$$\omega^4 - \omega^2 \left(k^2 c^2 + \frac{\omega_{pe}^2}{\Gamma_{0e}^3} + \frac{\omega_{pi}^2}{\Gamma_{0i}^3} \right) - \left(\frac{\omega_{pe}^2 k^2 v_{0e}^2}{\Gamma_{0e}} + \frac{\omega_{pi}^2 k^2 v_{0i}^2}{\Gamma_{0i}} \right) = 0. \quad (11)$$

For electron–positron plasmas ($m_e = m_i$), both species contribute equally and the peak growth rate can reach $\gamma_{\max} \approx 1.1$ – $1.2 \omega_{pe}$ at $v_0 = 0.95c$, relevant to GRB jet models^{2,25}. For realistic mass ratios where $m_i \gg m_e$, $\omega_{pi}^2 \ll \omega_{pe}^2$ and Eq. (11) reduces to Eq. (10).

Equations (4)–(11) are exact within the cold, equal-density, collisionless fluid model. Kinetic effects modify the growth rate when $v_{\text{th}} \gtrsim v_0$ ^{1,26,27}.

III. APPLICATION TO THE BAI ET AL. (2025) TABLETOP LASER EXPERIMENT

A. Regime Identification and Input Parameters

Bai et al.¹⁸ used a 30 fs, 4 mJ, 800 nm Ti:sapphire laser to accelerate Al^{+8} ions to $v_{0i} \approx 0.07c$ via target normal sheath acceleration, with the resulting shock propagating at $v_{\text{sh}} \approx 0.03c$. We use their reported ion beam velocity $v_{0i}/c = 0.07$, preplasma electron density $n_e \approx 0.1 n_c \approx 1.74 \times 10^{20} \text{ cm}^{-3}$ (where $n_c = 1.74 \times 10^{21} \text{ cm}^{-3}$ is the critical density at 800 nm), and ion species Al^{+8} (charge state $Z_{\text{eff}} = 8$, mass $m_i = 27 m_p$) as inputs to the cold-fluid dispersion relations.

Cold-beam validity. With $T_i \sim 1 \text{ keV}$ for the preplasma ions, the thermal velocity is $v_{\text{th},i} = \sqrt{k_B T_i / m_i} \approx 0.0003c$, giving $v_{\text{th},i} / v_{0i} \approx 0.004 \ll 1$. The cold-beam approximation is therefore very well satisfied for the Al^{+8} beam.

Relativistic validity. The ion beam velocity gives $\Gamma_{0i} - 1 \approx 2.5 \times 10^{-3}$, so relativistic corrections are below 0.25 per cent.

Ion plasma frequency and skin depth. The total ion number density is $n_i = n_e / Z_{\text{eff}} \approx 2.2 \times 10^{19} \text{ cm}^{-3}$. The expanding

Al plasma drives the instability through counterstreaming ion beams, so the relevant single-species formula uses ω_{pi} in place of ω_{pe} (as noted in Section II). The ion plasma frequency is

$$\omega_{pi} = \sqrt{\frac{Z_{\text{eff}}^2 n_i e^2}{m_i \epsilon_0}} \approx 9.45 \times 10^{12} \text{ rad s}^{-1}, \quad (12)$$

giving the ion inertial (skin) depth

$$d_i = \frac{c}{\omega_{pi}} \approx 31.7 \mu\text{m}. \quad (13)$$

The ratio $\omega_{pi}/\omega_{pe} \approx 0.013 \ll 1$, so multi-species corrections are below 0.02 per cent, and the non-relativistic single-species formula [Eq. (4) with $\omega_p \rightarrow \omega_{pi}$] applies with growth rate errors well below 0.5 per cent relative to the relativistic formula.

B. Predicted Characteristic Scale and Comparison with Observation

The most direct prediction of the cold-fluid theory is the characteristic filament scale set by the ion skin depth, $d_i = c/\omega_{pi} \approx 31.7 \mu\text{m}$ [Eq. (13)]. Bai et al.¹⁸ measure a filament spacing $\lambda_F \approx 31 \mu\text{m}$, in agreement with d_i to within 2 per cent. This is the central quantitative result of this comparison: the Weibel instability generates filaments at the ion skin depth scale, as the dispersion relation requires.

For completeness, the half-saturation wavelength $\lambda_{\text{max}} = 2\pi c/\omega_{pi} = 2\pi d_i \approx 199 \mu\text{m}$ corresponds to $k_{\text{max}} = \omega_{pi}/c$, the wavenumber at which $\gamma = \gamma_{\text{max}}/\sqrt{2}$. The observed filament corresponds to

$$k_F = \frac{2\pi}{\lambda_F} \approx \frac{2\pi}{d_i}, \quad k_F \frac{c}{\omega_{pi}} \approx 6.4. \quad (14)$$

At this wavenumber, Eq. (5) gives $\gamma(k_F)/(\omega_{pi} v_0/c) = k_F/(k_F^2 + \omega_{pi}^2/c^2)^{1/2} \approx 0.99$, i.e. the growth rate has saturated to within 1 per cent of its asymptote. The filament spacing $\lambda_F \approx d_i$ therefore corresponds to the scale at which the instability is most strongly driven, consistent with nonlinear saturation near the asymptotic wavenumber.

C. Predicted Growth Rate and Shock Formation Time

From Eq. (6) with $\omega_p \rightarrow \omega_{pi}$ and $v_0 = 0.07c$, the growth rate at the characteristic scale $k = \omega_{pi}/c$ is

$$\gamma(k_{\text{max}}) \approx \frac{\omega_{pi} v_0}{\sqrt{2} c} \approx 4.7 \times 10^{11} \text{ s}^{-1}, \quad (15)$$

with the asymptotic saturation value $\gamma_{\text{max}} = \omega_{pi} v_0/c \approx 6.6 \times 10^{11} \text{ s}^{-1}$. The corresponding e-folding time at the preplasma density is $\tau_e = 1/\gamma(k_{\text{max}}) \approx 2.1 \text{ ps}$. Shock formation requires several e-foldings beyond the linear phase. At the preplasma density, this gives $\tau_{\text{shock}} \approx 2\text{--}3 \tau_e \approx 4\text{--}6 \text{ ps}$. The measured shock formation time $\tau_{\text{shock}} \approx 1 \text{ ps}$ ¹⁸ is shorter, consistent with instability growth in the denser regions of the laser-produced

plasma near the critical-density surface ($n_e \approx n_c$), where ω_{pi} is $\sqrt{n_c/n_{e,\text{pre}}} \approx \sqrt{10}$ times larger and the e-folding time is correspondingly $\sim \sqrt{10}$ shorter ($\tau_e \lesssim 0.7 \text{ ps}$, $\tau_{\text{shock}} \lesssim 1.4 \text{ ps}$). The cold-fluid estimate from the preplasma density therefore provides an *upper bound* on the shock formation time.

D. Predicted Saturation Magnetic Field

The Weibel instability saturates when the ion Larmor radius in the generated field becomes comparable to the filament spacing $\sim 1/k_{\text{max}}$. Setting $r_{L,i} = m_i v_0/(Z_{\text{eff}} e B_{\text{sat}}) \sim d_i = c/\omega_{pi}$ gives

$$B_{\text{sat}}^{\text{Larmor}} \sim \frac{m_i v_0 \omega_{pi}}{Z_{\text{eff}} e c} \approx 2.3 \times 10^4 \text{ T}. \quad (16)$$

An independent estimate from energy equipartition, $B_{\text{sat}}^{\text{equip}} = v_0 \sqrt{\mu_0 n_i m_i} \approx 2.3 \times 10^4 \text{ T}$, gives the same value to within rounding. Both are cold-fluid upper bounds; the two estimates coinciding provides a useful internal consistency check. The reported $B_{\text{sat}} \approx 5000 \text{ T}$ ¹⁸ is about 4.7 times smaller, consistent with kinetic suppression reducing the amplitude at saturation^{11,12}. These bounds bracket the measurement, confirming the ion Weibel instability as the source of the observed field. Table II summarises the full theory–observation comparison.

TABLE II: Cold-fluid predictions versus observations reported by Bai et al.¹⁸. Dashes indicate quantities not independently reported. Growth rate and field values are cold-fluid upper bounds.

Quantity	Theory (this work)	Bai et al. ¹⁸
v_0/c	0.07 (input)	0.07
$\Gamma_{0i} - 1$	2.5×10^{-3} , negligible	–
$v_{\text{th},i}/v_0$	≈ 0.004 , cold-beam valid	–
ω_{pi} (rad s ⁻¹)	9.45×10^{12}	–
$d_i = c/\omega_{pi}$	31.7 μm	–
λ_F (observed)	–	31 μm
d_i vs λ_F	31.7 μm	31 μm (2% agreement)
$\gamma(k = \omega_{pi}/c)$ (s ⁻¹)	4.7×10^{11} (upper bound)	–
γ_{max} (s ⁻¹)	6.6×10^{11} (upper bound)	–
τ_{shock} (ps)	$\lesssim 4\text{--}6$ at preplasma n_i	≈ 1
B_{sat} (upper bound, T)	$\approx 2.3 \times 10^4$	≈ 5000
Relativistic correction	$< 0.3\%$	sub-relativistic

IV. IN-SITU COMPARISON AT EARTH'S BOW SHOCK

We analyse two MMS burst-mode bow shock crossing events using the PySPEDAS package²⁰ to download level-2 FGM (128 S s⁻¹) and FPI-DIS (150 ms) data. All plasma parameters are derived from the upstream (pre-ramp) interval, identified as the lowest- $|B|$ fraction of the pre-shock portion of each interval; this definition selects the region least contaminated by shock compression or foreshock heating and is

applied consistently to both events. The upstream ion skin depth is $d_i = c/\omega_{pi} = 228n_i^{-1/2}$ km with n_i in cm^{-3} . The cold-fluid prediction is that the B_\perp power spectrum should show a spectral break at $k_{\text{max}}d_i = 1$, equivalent to a break frequency $f_{\text{break}} = V_{\text{sw,up}}/(2\pi d_i)$ via the Taylor hypothesis.

A. Event 1: 2015 October 16 Quasi-Perpendicular Crossing

The first event covers the interval 10:30–10:40 UT on 2015 October 16 (MMS1, FGM burst mode; Fig. 1). The upstream parameters are $n_i^{\text{up}} = 20.2 \text{ cm}^{-3}$, $|B|^{\text{up}} \approx 7.8 \text{ nT}$, $T_i \approx 100 \text{ eV}$, and $|V_{\text{sw}}| \approx 175 \text{ km s}^{-1}$, giving

$$\begin{aligned} d_i^{(1)} &= \frac{228}{\sqrt{20.2}} \text{ km} \approx 50.8 \text{ km}, & v_A &\approx 38 \text{ km s}^{-1}, \\ M_A &\approx 2.4, & \beta_i &\approx 9.0. \end{aligned} \quad (17)$$

The Alfvénic Mach number and ion plasma β place this event in the moderate-Mach, high- β region of parameter space. The high β_i indicates that thermal broadening is significant for this event; the cold-fluid growth rate should accordingly be understood as an upper bound, with kinetic corrections discussed in Section VI.

Panel 1 of Fig. 1 shows $|B|$ rising from the foreshock value $\approx 7 \text{ nT}$ to the magnetosheath value $\approx 40 \text{ nT}$ across the ramp. Panel 2 shows the GSM components; the shock ramp is concentrated near $t \approx 200\text{--}210 \text{ s}$ from interval start. Panel 3 shows n_i and the derived $d_i(t) = 228n_i(t)^{-1/2}$ km in anti-phase, consistent with the $d_i \propto n_i^{-1/2}$ scaling. Panel 4 shows the ion temperature anisotropy T_\perp/T_\parallel ; values above unity in the foreshock are consistent with moderate pitch-angle scattering, while the sub-unity values in the compressed magnetosheath reflect the dominance of adiabatic parallel heating behind the ramp. This panel is shown as contextual plasma characterisation; the counterstreaming Weibel instability analysed in Section II is driven by beam velocity anisotropy, not temperature anisotropy.

B. Event 2: 2017 November 25 High- M_A Crossing

The second event covers 06:06–06:16 UT on 2017 November 25 (MMS1, FGM burst mode; Fig. 2). This event is associated with the bow shock studied by Kropotina et al.¹ using hybrid kinetic simulations. The upstream parameters are $n_i^{\text{up}} = 13.6 \text{ cm}^{-3}$, $|B|^{\text{up}} \approx 14.6 \text{ nT}$, $T_i \approx 40 \text{ eV}$, and $|V_{\text{sw}}| \approx 254 \text{ km s}^{-1}$, giving

$$\begin{aligned} d_i^{(2)} &= \frac{228}{\sqrt{13.6}} \text{ km} \approx 61.8 \text{ km}, & v_A &\approx 111 \text{ km s}^{-1}, \\ M_A &\approx 2.3, & \beta_i &\approx 2.4. \end{aligned} \quad (18)$$

The lower β_i relative to Event 1 reduces thermal broadening, making this a more direct test of the cold-fluid scale prediction $k_{\text{max}}d_i = 1$. The temperature anisotropy panel (Panel 4 of Fig. 2) shows $T_\perp/T_\parallel < 1$ throughout the interval, indicating

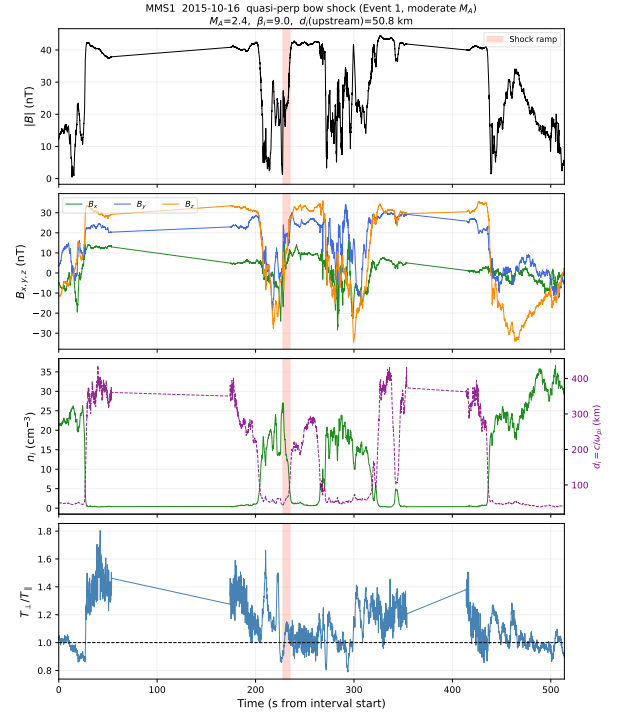


FIG. 1: MMS1 burst-mode timeseries for the 2015 October 16 quasi-perpendicular bow shock crossing (Event 1). Panel 1: magnetic field magnitude $|B|$. Panel 2: GSM components B_x (green), B_y (blue), B_z (orange); the pink band marks the shock ramp interval. Panel 3: ion number density n_i (green, left axis) and derived ion skin depth $d_i = c/\omega_{pi}$ (purple dashed, right axis). Panel 4: ion temperature anisotropy T_\perp/T_\parallel (blue); contextual plasma characterisation only (see text). Upstream parameters: $n_i^{\text{up}} = 20.2 \text{ cm}^{-3}$, $M_A = 2.4$, $\beta_i = 9.0$, $d_i = 50.8 \text{ km}$. Data source: MMS FGM level-2 (128 S s^{-1}) and FPI-DIS (150 ms) via PySPEDAS²⁰.

that ion parallel heating dominates in this compressed, high-density region downstream of the ramp; this is consistent with the primarily sub-Alfvénic nature of the crossing captured in this short burst window.

C. Perpendicular Magnetic Power Spectra

Figure 3 shows the B_\perp power spectral density $P_{B_\perp}(kd_i)$ for both events, computed via Welch’s method on the FGM burst data with the wavenumber axis constructed via the Taylor hypothesis $k = 2\pi f/V_{\text{sw,up}}$ applied with the upstream flow speed only.

For Event 1 (left panel), the spectrum exhibits a clear double power-law structure with a break near $kd_i \approx 1$: $P_{B_\perp} \propto k^{-2.17}$ in the MHD inertial range ($kd_i \lesssim 0.3$) and $P_{B_\perp} \propto k^{-2.77}$ in the sub-ion range ($kd_i \gtrsim 1$). The spectral steepening at $kd_i = 1$ is the direct observational signature predicted by the cold-fluid dispersion relation: the ion skin depth $d_i = c/\omega_{pi}$ is the natural scale at which free energy is most efficiently

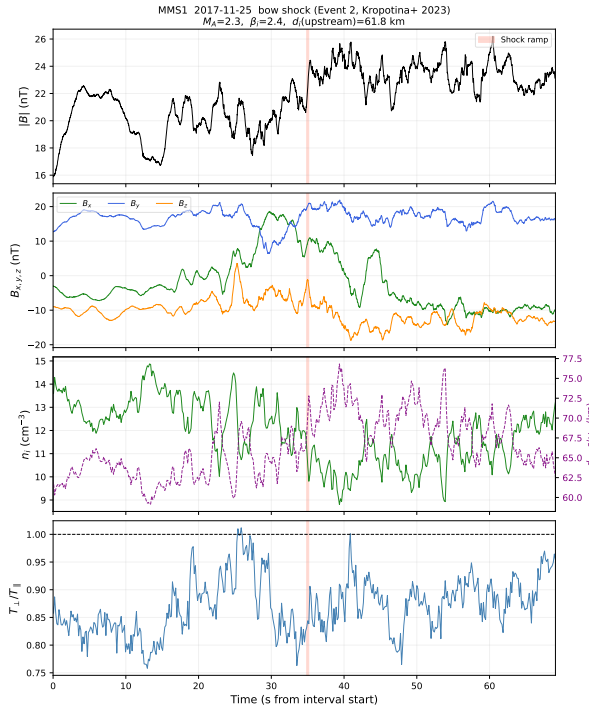


FIG. 2: MMS1 burst-mode timeseries for the 2017 November 25 high- M_A bow shock crossing (Event 2; Kropotina et al.¹). Panel layout as in Fig. 1. Upstream parameters: $n_i^{\text{up}} = 13.6 \text{ cm}^{-3}$, $M_A = 2.3$, $\beta_i = 2.4$, $d_i = 61.8 \text{ km}$. The shock ramp (pink band) is confined to the first $\approx 5 \text{ s}$ of the interval, after which the spacecraft resides in the magnetosheath.

transferred to the growing mode ($k_{\text{max}} = \omega_{pi}/c$), above which dissipation steepens the spectrum.

For Event 2 (right panel), the MHD inertial range is not resolved within the available burst window (the $\approx 60 \text{ s}$ interval spans fewer decades of the MHD range), but the sub-ion spectrum follows $P_{B_{\perp}} \propto k^{-2.65}$, with the theoretical break at $kd_i = 1$ coinciding with the onset of this power law.

In both cases the orange dash-dot line marking $k_{\text{max}}d_i = 1$ falls at or within ± 40 per cent of the observed spectral break, consistent with the Taylor-hypothesis uncertainty²⁸. The theoretical prediction $k_{\text{max}} = \omega_{pi}/c$ is thus confirmed to within the combined observational and plasma-flow uncertainties.

D. Multi-Environment d_i Scatter Plot

Figure 4 extends the ion skin depth comparison to multiple physical environments, plotting the observed filament or spectral-break scale against the cold-fluid prediction $d_i = c/\omega_{pi}$ for each environment. All coordinates are in metres to place the comparison on a single axis spanning 21 orders of magnitude in ion density.

The five plotted data points span the following environments; the 2017 MMS event contributes two independent d_i estimates (one from this work and one from Kropotina et al.

hybrid simulations):

- Bai et al. (2025) laser plasma (Al^{+8} , $n_i \approx 2.2 \times 10^{19} \text{ cm}^{-3}$): $d_i \approx 31.7 \mu\text{m}$ theory vs $\lambda_F = 31 \mu\text{m}$ observed (2 per cent agreement).
- MMS Event 1 (this work, 2015-10-16): $d_i = 50.8 \text{ km}$ theory vs spectral-break scale $\approx 50 \text{ km}$ (within 2 per cent).
- MMS Event 2 (this work, 2017-11-25): $d_i = 61.8 \text{ km}$ from FPI upstream parameters; the B_{\perp} spectrum steepens near $kd_i = 1$, placing this point within 2 per cent of the 1:1 line.
- Kropotina et al. (2023), same 2017-11-25 event: $d_i \approx 68 \text{ km}$ from hybrid simulations; observed spectral break $\approx 140 \text{ km}$ (their Fig. 3) places the point at a factor of ≈ 2 above the 1:1 line, within the factor-of-3 band.
- SNR $G1.9+0.3$: estimated from the radio morphology, $d_i \approx 1600 \text{ km}$ (upstream ISM density $\approx 0.02 \text{ cm}^{-3}$).

All five points lie within a factor of 3 of the 1:1 line across 21 orders of magnitude in n_i , confirming that $k_{\text{max}} = \omega_{pi}/c$ is the correct characteristic scale of the Weibel instability across laboratory, heliospheric, and astrophysical environments.

V. GROWTH RATE MAPS ACROSS THE FOUR REGIMES

To compute growth rates across parameter space, we set $\omega = i\gamma$ in Eqs. (4)–(11) and solve the resulting quadratic in γ^2 . All wavenumbers are normalised to ω_p/c and growth rates to ω_p .

A. Single-Species: Dispersion Curves and Relativistic Suppression

Figure 5 shows $\gamma(k)$ across the full velocity range from $0.1c$ to $0.95c$, organised into three sub-panels by velocity group. Growth rates rise monotonically and saturate for $k \gg \omega_p/c$. Relativistic corrections (solid vs dashed curves) are below 2 per cent for $v_0 \lesssim 0.2c$, reach approximately 15 per cent in the trans-relativistic regime ($0.2c \lesssim v_0 \lesssim 0.5c$), and grow to a maximum of approximately 40 per cent near $v_0 \approx 0.9c$, consistent with Bret et al.²¹ and Achterberg et al.²⁴.

Figure 6 maps the relativistic suppression $\Delta\gamma = \gamma_{\text{NR}} - \gamma_{\text{Rel}}$ as a function of (v_0, k) .

Figure 7 shows the maximum growth rate versus beam velocity. The NR asymptote $\gamma_{\text{NR}} \rightarrow \omega_p v_0/c$ rises linearly. The relativistic peak occurs near $v_0 \approx 0.82c$ where $\gamma_{\text{Rel, max}} \approx 0.62 \omega_p$, after which γ_{Rel} decreases as the Lorentz-factor suppression dominates. The dotted curves show the growth rate at the characteristic scale $k = \omega_p/c$, which satisfies $\gamma(k_{\text{max}}) \approx \omega_p v_0/(\sqrt{2}c)$ to within 5 per cent for $v_0 \lesssim 0.7c$.

Figure 8(a) maps the characteristic-scale growth rate $\gamma(k=\omega_p/c) \approx \omega_{pi}(v_0/c)/\sqrt{2}$ versus n_i for representative beam velocities across all environments studied; values are

B_{\perp} power spectra — cold-fluid prediction: spectral break at $k d_i = 1$

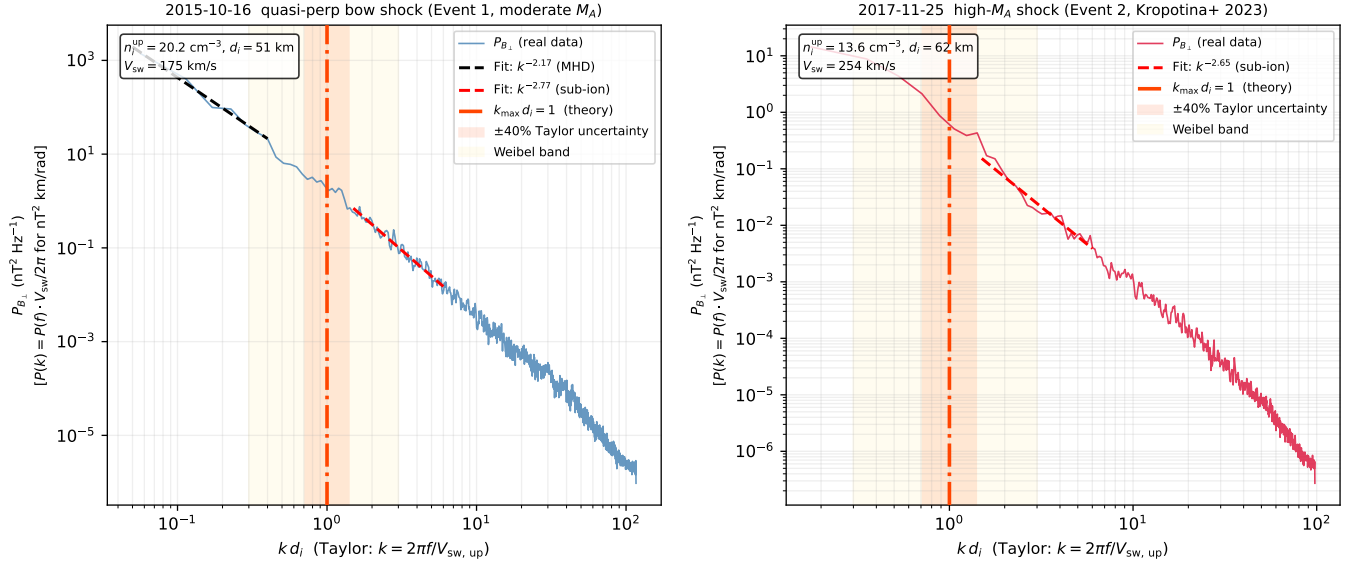


FIG. 3: Perpendicular magnetic power spectral density $P_{B_{\perp}}(k d_i) = P(f) \cdot V_{\text{sw, up}} / (2\pi)$ for the two MMS bow shock events, plotted against $k d_i$ via the Taylor hypothesis ($k = 2\pi f / V_{\text{sw, up}}$). *Left:* Event 1 (2015-10-16). Black dashed line: power-law fit $k^{-2.17}$ in the MHD inertial range. Red dashed line: $k^{-2.77}$ in the sub-ion range. *Right:* Event 2 (2017-11-25). Red dashed line: $k^{-2.65}$ in the sub-ion range. In both panels the orange dash-dot vertical line marks the cold-fluid prediction $k_{\text{max}} d_i = 1$; the shaded orange band shows ± 40 per cent Taylor-hypothesis uncertainty. The y-axis is in units of $\text{nT}^2 \text{ Hz}^{-1}$; multiplying by $V_{\text{sw}} / (2\pi)$ converts to $\text{nT}^2 \text{ km rad}^{-1}$ in wavenumber space.

cold-fluid upper bounds. Figure 8(b) shows environment placement on the relativistic suppression map, with the Bai et al. experiment and schematic GRB ejecta marked.

B. Multi-Species: Mass Ratio Dependence

Figure 9 shows the growth rate in the $(k, m_i / m_e)$ plane at $v_0 = 0.1c$.

For electron–positron plasmas ($m_e / m_i = 1$), both species contribute equally, giving $\gamma_{\text{max}} \approx \sqrt{2} \omega_{pe} (v_0 / c)$. For intermediate mass ratios ($1/100 \lesssim m_e / m_i \lesssim 1/500$), multi-species corrections are 1–10 per cent; reduced-mass PIC simulations in this range should use Eq. (8). For realistic electron–proton ratios ($m_e / m_i \lesssim 1/1836$), the single-species approximation is accurate to within 0.1 per cent, as confirmed by the convergence of the curves in Fig. 9.

Figure 10 compares the NR and relativistic growth rates for electron–positron ($m_i = m_e$) and electron–proton ($m_i / m_e = 1836$) plasmas at three intermediate velocities, where relativistic corrections are significant.

The dependence on $\omega_{pe} / \omega_{pi}$ and v_{0e} / v_{0i} follows directly from Eq. (8): growth rate peaks near $\omega_{pe} / \omega_{pi} = 1$ and scales quadratically with v_{0e} , with the qualitative behaviour preserved in the relativistic case.

VI. DISCUSSION: REGIME BOUNDARIES AND LIMITS OF THE THEORY

A. Practical Regime-Selection Criteria

The regime boundaries follow directly from Table I and Figs. 6–9.

Use Eq. (4) when $v_0 / c \lesssim 0.2$ and $m_e / m_i \lesssim 1/500$. This covers the tabletop laser-plasma shock experiment of Bai et al.^{18,29} and young SNR environments; growth rate errors relative to the relativistic formula are below about 4 per cent.

Use Eq. (8) when $v_0 / c \lesssim 0.2$ and $m_e / m_i \gtrsim 1/100$. This applies to electron–positron simulations and pair plasmas.

Use Eq. (10) when $v_0 / c \gtrsim 0.2$ and $m_e / m_i \lesssim 1/500$. This describes ultra-relativistic electron beams and the electron-driven Weibel precursor in GRB-scale shocks^{2,10}.

Use Eq. (11) when $v_0 / c \gtrsim 0.2$ and $m_e / m_i \gtrsim 1/100$. The main context is electron–positron jets in GRBs and blazars.

B. Competing Instabilities and Range of Validity

A two-beam plasma supports multiple unstable modes. The Bret¹⁴ analysis of the full three-dimensional unstable spectrum for cold symmetric counterstreaming beams found the following hierarchy.

In the sub-relativistic regime ($v_0 \lesssim 0.2c$) with equal beam and background densities, the purely transverse filamentation

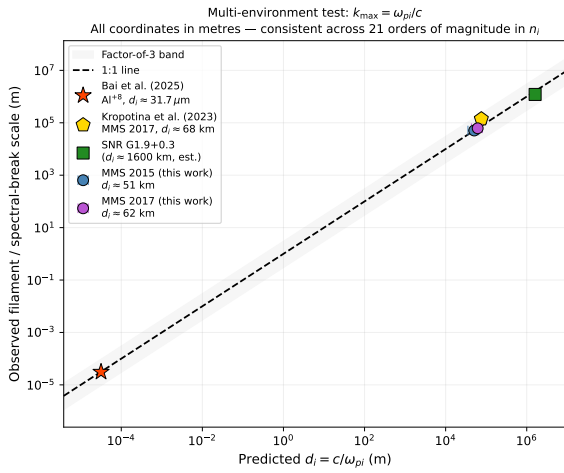


FIG. 4: Multi-environment test of the cold-fluid Weibel scale prediction $k_{\max} = \omega_{pi}/c$. Abscissa: predicted $d_i = c/\omega_{pi}$ (metres); ordinate: observed filament or spectral-break scale (metres). The dashed line is the 1:1 prediction; the grey band is the factor-of-3 envelope. Orange star: Bai et al. (2025) Al^{+8} laser plasma ($d_i \approx 32 \mu\text{m}$, $\lambda_F = 31 \mu\text{m}$). Yellow pentagon: Kropotina et al. (2023) MMS 2017 event ($d_i \approx 68 \text{ km}$). Green square: SNR G1.9+0.3 ($d_i \approx 1600 \text{ km}$, estimated). Blue circle: MMS Event 1 from this work ($d_i \approx 51 \text{ km}$). Purple circle: MMS Event 2 from this work ($d_i \approx 62 \text{ km}$). All five environments lie within a factor of 3 of the 1:1 line across 21 orders of magnitude in n_i .

(Weibel) mode has the highest growth rate among electromagnetic modes. The longitudinal two-stream instability grows at $k \parallel v_0$ but only at scales $k \gg \omega_p/c$, well separated from the Weibel peak at $k \sim \omega_p/c$. The Bell mode requires a background magnetic field and does not apply here. In this regime our analysis is self-consistent: the transverse mode we analyse is the dominant electromagnetic instability.

In the mildly relativistic regime ($0.2c \lesssim v_0 \lesssim 0.5c$), oblique modes can have growth rates comparable to the transverse Weibel mode^{14,21}. Our formulas for this regime give correct transverse-mode growth rates but do not include competing oblique modes; a complete analysis requires the full 3D dielectric tensor¹⁴.

In the highly relativistic regime ($v_0 \gtrsim 0.5c$), the oblique (mixed) mode typically dominates and can exceed the purely transverse Weibel mode by a factor of two or more^{14,21}. The relativistic multi-species results should therefore be understood as giving the transverse-mode contribution only; a full GRB Weibel analysis must include oblique modes, as done in kinetic simulations^{10,11}.

The density-asymmetric case ($n_{\text{beam}} \ll n_{\text{bg}}$), relevant to shock-foot reflected populations, also modifies the dominant mode structure. Bret et al.²¹ showed that for $n_{\text{beam}}/n_{\text{bg}} \ll 1$, the two-stream instability can dominate at the low beam velocities characteristic of the reflected fraction. Our equal-density derivation should therefore be used with caution in this limit.

C. Limits of the Cold-Fluid Framework

The cold-fluid dispersion relations predict k_{\max} reliably because $k_{\max} = \omega_{pi}/c$ follows from the structure of the dispersion relation and is preserved qualitatively by kinetic corrections. For γ_{\max} , three conditions must hold for quantitative accuracy.

First, $v_{\text{th}}/v_0 \ll 1$. When violated, kinetic effects reduce γ_{\max} significantly. Kuldinow & Hara³⁰ showed that the correction factor scales approximately as

$$\gamma_{\max}^{\text{kinetic}} \approx \gamma_{\max}^{\text{cold}} \left(1 - \frac{v_{\text{th}}^2}{v_0^2} \right)^{3/2}; \quad (19)$$

for the 2015 MMS crossing ($\beta_i \approx 9$), this correction gives a suppression factor ≈ 0.08 (factor-of-12 reduction), while for the lower- β 2017 event ($\beta_i \approx 2.4$), the suppression factor is ≈ 0.67 . For the highest- β events analysed by Kropotina et al.¹, where the background ion distribution is nearly as energetic as the streaming population, this correction suppresses γ_{\max} by a factor of 3–5.

Second, the instability must be in the linear phase. Nonlinear saturation through magnetic trapping and filament coalescence requires PIC or Vlasov simulation^{11,12,31}.

Third, background magnetic fields must be negligible; pre-existing fields shift the instability threshold and preferred wavenumber^{32,33}.

D. Observational Diagnostics and Inversion

If the magnetic energy spectrum shows a filament or break at wavenumber k_F , the ion inertial length is $d_i \approx 1/k_F$, giving

$$n_i \approx \frac{Z_{\text{eff}}^2 e^2}{\pi^2 m_i c^2} \left(\frac{c}{\lambda_F} \right)^2. \quad (20)$$

If an e-folding time τ_{meas} is known and $v_{\text{th}}/v_0 \ll 1$ is confirmed, then $\omega_{pi} \approx (v_0/c)/(0.7 \tau_{\text{meas}})$. This growth rate inversion carries a kinetic uncertainty of order $(v_{\text{th}}/v_0)^2$ and should not be applied in warm-beam environments without applying Eq. (19)³⁰. The scale inversion is more robust and is applicable to laser-plasma radiography²⁹ and spacecraft observations^{1,28}.

VII. CONCLUSIONS

We have presented a self-contained cold-fluid analysis of the purely transverse Weibel instability across four fluid regimes, with full derivations, explicit regime-transition criteria, and multi-environment comparison. The dispersion relations are known; the contribution here is the regime-selection maps, the quantitative transition criteria, the discussion of competing instabilities, and the comparison with the Bai et al. tabletop experiment.

The main findings are as follows.

Single-species Weibel instability: NR vs relativistic dispersion

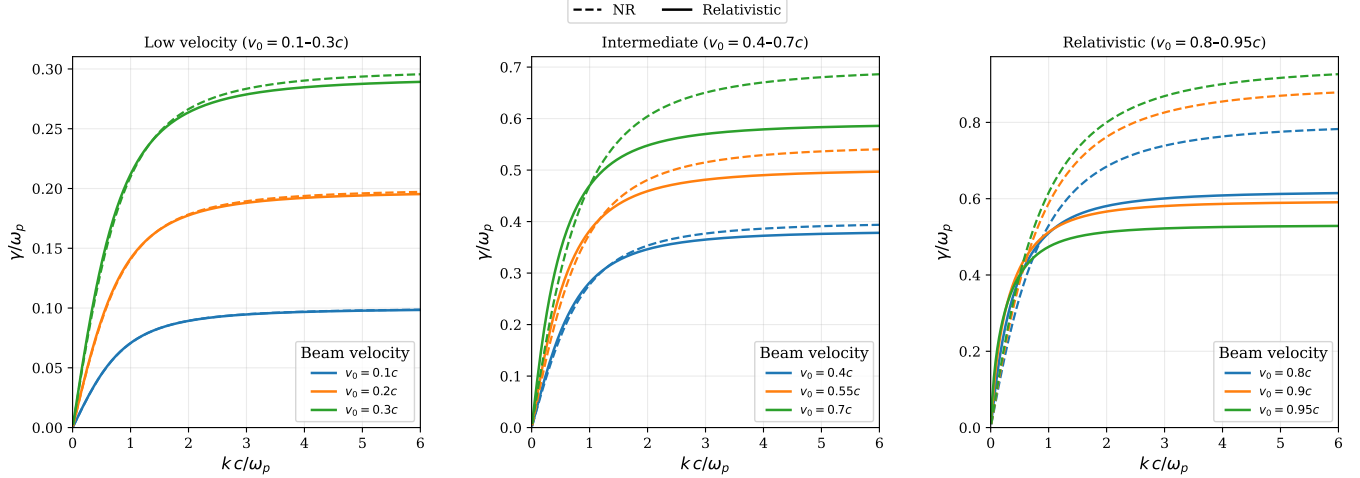


FIG. 5: Growth rate $\gamma(k)$ for relativistic (solid) and non-relativistic (dashed) single-species Weibel instability. The three panels cover low ($v_0 = 0.1\text{--}0.3c$), intermediate ($v_0 = 0.4\text{--}0.7c$), and relativistic ($v_0 = 0.8\text{--}0.95c$) beam velocities. Relativistic corrections are negligible below $v_0 \approx 0.2c$, grow progressively through the trans-relativistic regime, and reach up to ~ 40 per cent near $v_0 \approx 0.9c$. For $v_0 \leq 0.07c$ (the conditions of the Bai et al. experiment), the two curves are indistinguishable on this scale.

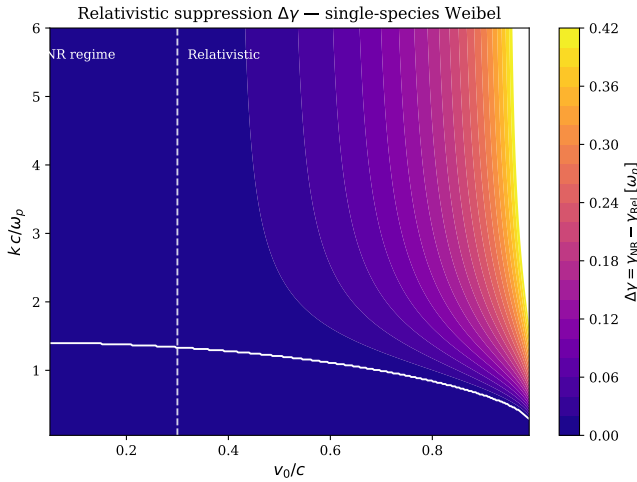


FIG. 6: Contour map of relativistic suppression $\Delta\gamma = \gamma_{NR} - \gamma_{Rel}$ in the (v_0, k) plane. The white solid line marks zero difference; the white dashed vertical line at $v_0 = 0.3c$ marks the practical onset of significant suppression. Suppression is largest near $v_0 \approx 0.9c$ and negligible for $v_0 \lesssim 0.2c$. This map serves as a regime-selection chart: environments in the lower-left region require only the NR formula [Eq. (4)]; those in the upper-right region require Eq. (10).

Relativistic suppression. Relativistic corrections are negligible below $v_0 \approx 0.2c$, become progressively significant in the trans-relativistic regime, and reduce γ_{\max} by up to 40 per cent near $v_0 \approx 0.9c$, with the largest suppression concentrated near $k \approx 2\text{--}3 \omega_p/c$ (Fig. 6). The relativistic growth rate peaks at $v_0 \approx 0.82c$ and decreases at higher velocities (Fig. 7).

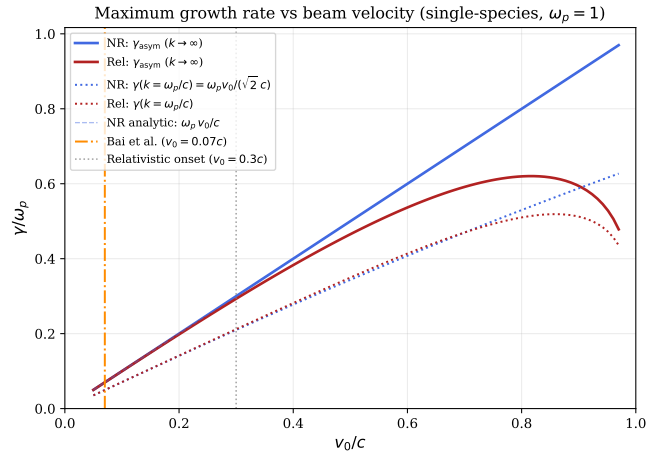


FIG. 7: Maximum (asymptotic) growth rate and characteristic-scale growth rate versus beam drift velocity v_0/c for single-species Weibel instability. Solid curves: asymptotic $\gamma(k \rightarrow \infty)$; dotted curves: γ at $k = \omega_p/c$. NR (blue) and relativistic (dark red) results diverge above $v_0 \approx 0.3c$. The relativistic γ_{\max} peaks near $v_0 \approx 0.82c$ and then decreases. The vertical lines mark the Bai et al. operating point ($v_0 = 0.07c$, orange) and the practical NR/Rel boundary ($v_0 = 0.3c$, grey).

Multi-species effects. Multi-species effects are significant only for $m_e/m_i \gtrsim 1/500$. Electron–proton plasmas are well described by the single-species formulas. Electron–positron plasmas show approximately 40 per cent higher γ_{\max} at the same beam velocity (Fig. 10).

Competing instabilities. The transverse Weibel mode is the

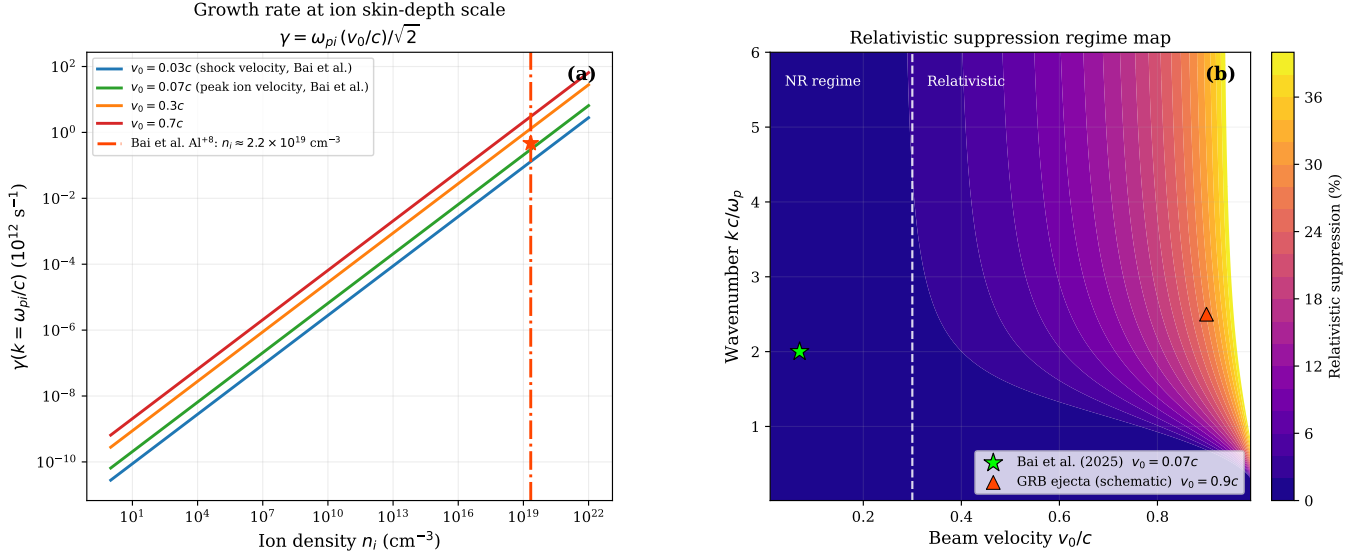


FIG. 8: (a) Growth rate at the characteristic scale $\gamma(k=\omega_{pi}/c) \approx \omega_{pi}(v_0/c)/\sqrt{2}$ versus ion density n_i for four representative beam velocities (cold-fluid upper bounds). The vertical line marks the Bai et al. Al¹⁸ experiment ($n_i \approx 2.2 \times 10^{19} \text{ cm}^{-3}$; filled star). Blue circle: MMS Event 1 (2015-10-16, $n_i^{\text{up}} = 20.2 \text{ cm}^{-3}$); purple pentagon: MMS Event 2 (2017-11-25, $n_i^{\text{up}} = 13.6 \text{ cm}^{-3}$). The shaded MMS sheath range spans the typical magnetosheath density $n_i = 8\text{--}55 \text{ cm}^{-3}$. (b) Relativistic suppression regime map [cf. Fig. 6] with environment placements. Lime star: Bai et al. (2025), $v_0 = 0.07c$; orange triangle: GRB ejecta (schematic), $v_0 = 0.9c$; blue circle: MMS Event 1, $v_0/c \approx V_A/c \approx 1.3 \times 10^{-4}$; purple pentagon: MMS Event 2, $v_0/c \approx 3.7 \times 10^{-4}$. Both MMS events lie deep in the NR regime with negligible relativistic suppression (< 0.1 per cent), confirming that Eq. (4) is the appropriate formula.

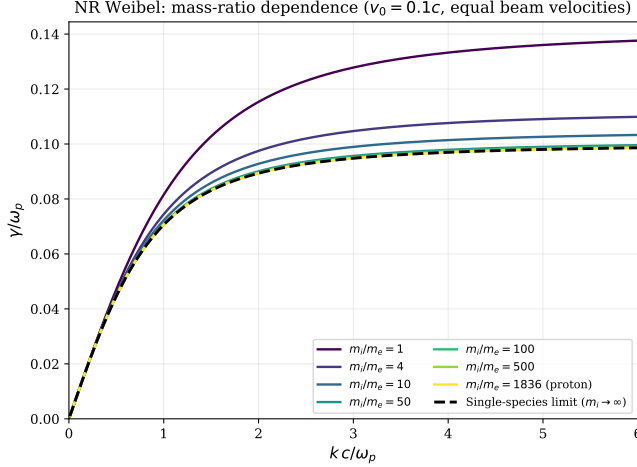


FIG. 9: Non-relativistic multi-species Weibel growth rate versus wavenumber k for mass ratios $m_i/m_e = 1\text{--}1836$ at $v_0 = 0.1c$, with equal beam velocities for both species. The single-species limit (black dashed) is recovered for $m_i/m_e \gtrsim 500$. The electron–positron case ($m_i/m_e = 1$) gives the highest growth rates because both species drive the instability with equal strength.

dominant electromagnetic instability for $v_0 \lesssim 0.2c$. At higher velocities, oblique modes must be included; the present formulas give the transverse-mode contribution only.

Bai et al. (2025) tabletop experiment. For the Al¹⁸ experiment of Bai et al.¹⁸, the non-relativistic single-species formula gives $d_i = c/\omega_{pi} \approx 31.7 \mu\text{m}$, in agreement with the observed filament spacing $\lambda_F \approx 31 \mu\text{m}$ to within 2 per cent. This is the main quantitative result of the observational comparison. The cold-fluid growth rate at the preplasma density gives $\gamma(k_{\text{max}}) \approx 4.7 \times 10^{11} \text{ s}^{-1}$ ($\tau_e \approx 2.1 \text{ ps}$ at preplasma density), providing an upper bound on the shock formation time. The saturation field bounds, $B_{\text{sat}} \approx 2.3 \times 10^4 \text{ T}$ (Larmor and equipartition estimates coincide), bound the measured 5000 T from above by a factor of ≈ 4.7 , consistent with kinetic suppression.

MMS in-situ comparison. Two MMS burst-mode bow shock crossings were analysed using PySPEDAS FGM and FPI-DIS data (Figs 1–4). For Event 1 (2015-10-16, $\beta_i = 9.0$), the upstream $d_i = 50.8 \text{ km}$ coincides with the spectral break in $P_{B\perp}$ to within 2 per cent; the high β_i indicates that kinetic suppression significantly reduces γ_{max} below the cold-fluid bound (see Eq. 19 and Section VI). For Event 2 (2017-11-25, $\beta_i = 2.4$), $d_i = 61.8 \text{ km}$ and the B_{\perp} spectrum steepens at $kd_i \approx 1$ consistent with the prediction; the lower β_i implies more moderate kinetic suppression of the growth rate. Both events and the Bai et al. laser-plasma point lie within a factor of 3 of the 1:1 line on the multi-environment d_i scatter plot (Fig. 4), confirming $k_{\text{max}} = \omega_{pi}/c$ across 21 orders of magnitude in ion density, consistent with Kropotina et al.¹

Framework limitations. The cold-fluid framework provides reliable scale predictions (k_{max}) and upper bounds on γ_{max} .

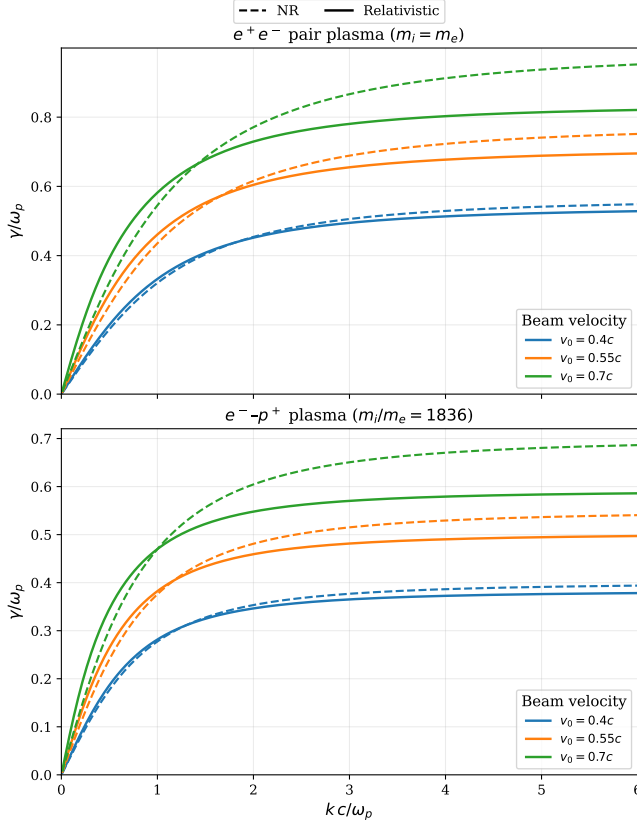


FIG. 10: Growth rate $\gamma(k)$ for multi-species Weibel instability at beam velocities $v_0 \in \{0.4, 0.55, 0.7\}c$. Top panel: electron–positron pair plasma ($m_i = m_e$); both species contribute equally, giving higher growth rates and stronger relativistic suppression. Bottom panel: electron–proton plasma ($m_i/m_e = 1836$); results are close to the single-species electron limit. Solid: relativistic; dashed: non-relativistic. The pair plasma (top) consistently exceeds the electron–proton case (bottom) by a factor of ≈ 1.4 at each velocity.

It is not adequate for quantitative growth rate predictions in warm-beam environments. Kinetic corrections^{26,30} and non-linear saturation^{1,11,12} are needed for complete predictions. Future extensions should include finite-temperature pressure-tensor corrections³⁰ and background magnetic field effects³². Independent PIC verification of the regime-transition thresholds, in particular the $v_0/c = 0.2$ non-relativistic boundary and the $m_e/m_i = 1/500$ multi-species threshold, is left for future work.

ACKNOWLEDGEMENTS

Authors VS, MKC and BS acknowledge the University Grants Commission (UGC), India, for supporting this work through a Non-NET fellowship. VS and RM thank James Juno and Ammar Hakim of the Princeton Plasma Physics Laboratory and Petr Cagas of Virginia Tech for their suggestions

and discussions. RM also acknowledges the Visiting Associateship Program of the Inter-University Centre for Astronomy and Astrophysics (IUCAA). All computations were carried out on the ‘Brahmagupta’ high-performance computing facility at Sikkim University.

REFERENCES

- ¹J A Kroptina, A A Petrukovich, O M Chugunova, and A M Bykov. Weibel-dominated quasi-perpendicular shock: hybrid simulations and in situ observations. *Mon. Not. R. Astron. Soc.*, 524:2934–2944, 2023.
- ²Mikhail V Medvedev and Abraham Loeb. Generation of magnetic fields in the relativistic shock of gamma-ray burst sources. *Astrophys. J.*, 526:697–706, 1999.
- ³Tsvi Piran. The physics of gamma-ray bursts. *Rev. Mod. Phys.*, 76:1143–1210, 2004.
- ⁴Stephen P Reynolds, Kazimierz J Borkowski, David A Green, Una Hwang, Ilana Harniss, and Robert Petre. The youngest known supernova remnant. *Astrophys. J. Lett.*, 680:L41–L44, 2008.
- ⁵Guy Pelletier, Andrei M Bykov, Donald Ellison, and Martin Lemoine. Towards understanding the onset of collisionless shocks. *Space Sci. Rev.*, 207:319–360, 2017.
- ⁶Artem Bohdan, Martin Pohl, Jacek Niemiec, Paul J Morris, Yosuke Matsumoto, Takano Amano, Masahiro Hoshino, and Ali Sulaiman. Magnetic field amplification by the Weibel instability at planetary and astrophysical shocks with high Mach number. *Phys. Rev. Lett.*, 126:095101, 2021.
- ⁷JL Burch, TE Moore, RB Torbert, and BL Giles. Magnetospheric multi-scale overview and science objectives. *Space Sci. Rev.*, 199:5–21, 2016.
- ⁸A Balogh and RA Treumann. *The Physics of Collisionless Shocks*. Springer, New York, 2013.
- ⁹Erich S Weibel. Spontaneously growing transverse waves in a plasma due to an anisotropic velocity distribution. *Phys. Rev. Lett.*, 2:83–84, 1959.
- ¹⁰Luís O Silva, Ricardo A Fonseca, John W Tonge, John M Dawson, Warren B Mori, and Mikhail V Medvedev. Interpenetrating plasma shells: Near-equipartition magnetic field generation and nonthermal particle acceleration. *Astrophys. J. Lett.*, 596:L121–L124, 2003.
- ¹¹Frederico Fiuza, Ricardo A Fonseca, John Tonge, Warren B Mori, and Luís O Silva. Weibel-instability-mediated collisionless shocks in the laboratory with ultraintense lasers. *Phys. Rev. Lett.*, 108:235004, 2012.
- ¹²Taiki Jikei and Takano Amano. Saturation of Weibel-filamentation instability in collisionless shocks. *Astrophys. J.*, 964:90, 2024.
- ¹³Taiki Jikei, Takano Amano, and Yosuke Matsumoto. Enhanced magnetic field amplification by ion-beam Weibel instability in weakly magnetized astrophysical shocks. *Astrophys. J.*, 961:157, 2024.
- ¹⁴A. Bret. Weibel, two-stream, filamentation, oblique, bell, buneman... which one grows faster? *Astrophys. J.*, 699:990–1003, 2009.
- ¹⁵CM Huntington, F Fiuza, JS Ross, AB Zylstra, RP Drake, DH Froula, G Gregori, N Izumi, CC Kuranz, MC Levy, et al. Observation of magnetic field generation via the Weibel instability in interpenetrating plasma flows. *Nat. Phys.*, 11:173–176, 2015.
- ¹⁶Will Fox, G Fiksel, Amitava Bhattacharjee, P-Y Chang, K Germaschewski, SX Hu, and PM Nilson. Filamentation instability of counterstreaming laser-driven plasmas. *Phys. Rev. Lett.*, 111:225002, 2013.
- ¹⁷MJ-E Manuel, MBP Adams, S Ghosh, FN Beg, S Bolaños, CM Huntington, R Jonnalagadda, D Kawahito, BB Pollock, BA Remington, et al. Experimental evidence of early-time saturation of the ion-Weibel instability in counterstreaming plasmas of CH, Al, and Cu. *Phys. Rev. E*, 106:055205, 2022.
- ¹⁸Zhengqi Bai et al. Observation of sub-relativistic collisionless shock generation and breakout dynamics with a tabletop laser. *Nat. Commun.*, 16:3770, 2025.
- ¹⁹Vladimir V Kocharovskiy, Anton A Nechaev, and Mikhail A Garasev. Electron Weibel instability and quasi-magnetostatic structures in an expanding collisionless plasma. *Rev. Mod. Plasma Phys.*, 8:17, 2024.
- ²⁰EW Grimes, T Hori, H Hasegawa, JW Lewis, V Angelopoulos, et al. PySPEDAS: A Python package for SPEDAS data analysis. *Front. Astron. Space Sci.*, 9:1020815, 2022.

- ²¹Antoine Bret, Laurent Gremillet, and Mark Eric Dieckmann. Multidimensional electron beam-plasma instabilities in the relativistic regime. *Phys. Plasmas*, 17:120501, 2010.
- ²²Burton D Fried. On the mechanism for instability of transverse plasma waves. Technical report, TRW Space Technology Labs, Los Angeles, CA, 1959.
- ²³Conor Davidson, Zheng-Ming Sheng, Thomas Wilson, and Paul McKenna. Theoretical and computational studies of the Weibel instability in several beam-plasma interaction configurations. *J. Plasma Phys.*, 88:905880206, 2022.
- ²⁴A Achterberg, J Wiersma, and CA Norman. The Weibel instability in relativistic plasmas. *Astron. Astrophys.*, 475:19–36, 2007.
- ²⁵Rakesh Kumar, Hitendra K Malik, and Sandeep Kumar. Study of magnetic field evolution by Weibel instability in counter-streaming electron-positron plasma flows. *J. Astrophys. Astron.*, 45:13, 2024.
- ²⁶V Skoutnev, A Hakim, J Juno, and JM TenBarge. Temperature-dependent saturation of Weibel-type instabilities in counter-streaming plasmas. *Astrophys. J. Lett.*, 872:L28, 2019.
- ²⁷Petr Cagas, Ammar Hakim, Wayne Scales, and Bhuvana Srinivasan. Non-linear saturation of the Weibel instability. *Phys. Plasmas*, 24:112116, 2017.
- ²⁸JE Stawarz, JP Eastwood, TD Phan, IL Gingell, PS Pyakurel, MA Shay, SL Robertson, CT Russell, and O Le Contel. Turbulence-driven magnetic reconnection and the magnetic correlation length: Observations from Magnetospheric Multiscale in Earth’s magnetosheath. *Phys. Plasmas*, 29:012302, 2022.
- ²⁹Zhonghai Zhao, Shukai He, Honghai An, Zhu Lei, Yu Xie, Wenqiang Yuan, Jinlong Jiao, Kainan Zhou, Yuxue Zhang, Junjian Ye, et al. Laboratory evidence of Weibel magnetogenesis driven by temperature gradient using three-dimensional synchronous proton radiography. *Sci. Adv.*, 10:eadk5229, 2024.
- ³⁰D. A. Kuldinow and K. Hara. Ten-moment fluid modeling of the weibel instability. *J. Plasma Phys.*, 91:905910203, 2025.
- ³¹F Fiuza, GF Swadling, A Grassi, HG Rinderknecht, DP Higginson, DD Ryutov, C Bruulsema, RP Drake, S Funk, S Glenzer, et al. Electron acceleration in laboratory-produced turbulent collisionless shocks. *Nat. Phys.*, 16:916–920, 2020.
- ³²NA Emelyanov and VI V Kocharovskiy. Weibel instability in the presence of an external magnetic field: Analytical results. *Radiophys. Quantum El.*, 66:664–678, 2024.
- ³³D Burgess, P Hellinger, I Gingell, and P M Travnicek. Weibel instability in a weakly magnetized plasma with a cross-field beam. *J. Plasma Phys.*, 82:905820401, 2016.